Noname manuscript No.
(will be inserted by the editor)

Automated Cell Classification and Visualization for Analyzing Remyelination Therapy

Koel Das · Aditi Majumder · Monica Siegenthaler · Hans Keirstead · M Gopi

Received: date / Accepted: date

Abstract Remyelination therapy is a state-of-the-art technique for treating spinal cord injury (SCI). Demyelination – the loss of myelin sheath that insulates axons, is a prominent feature in many neurological disorders resulting in SCI. This lost myelin sheath can be replaced by remyelination. In this paper, we propose an algorithm for efficient automated cell classification and visualization to analyze the progress of remyelination therapy in SCI. Our method takes as input the images of the cells and outputs a density map of the therapeutically important oligodendrocyte-remyelinated axons (OR-axons) which is used for efficacy analysis of the therapy. Our method starts with detecting cell boundaries using a robust, shape-independent algorithm based on isocontour analysis of the image at progressively increasing intensity levels. The detected boundaries of spatially clustered cells are then separated using Delaunay triangulation based contour separation method. Finally, the OR-axons are identified and a density map is generated for efficacy analysis of the therapy. Our efficient automated cell classification and visualization of remyelination analysis significantly reduces error due to human subjectivity. We validate the accuracy of our results by extensive cross-verification by the domain experts.

Koel Das
South Asian University,India
Tel.: +91-11-26741475
Fax: +91-11-26741741
E-mail: das.koel@gmail.com

Aditi Majumder · M Gopi
Department of Computer Science University of California, Irvine

Monica Siegenthaler
California Stem Cell, Inc, Irvine

Hans Kierstead
Department of Anatomy and Neurobiology University of California, Irvine

Keywords cell detection · geometric processing · progressive isocontour

1 Introduction

The loss of myelin sheath or Demyelintion results in the disruption of signals within the axons. It is one of the primary features in spinal cord injury (SCI) and neurodegenerative autoimmune diseases including multiple sclerosis (MS) [29,5,39,24,40,13,36]. The lost myelin sheath can be replaced by a process called remyelination which wraps myelin sheath around the demyelinated axons restoring the conduction of signals within the axons. Remyelination can be achieved by two kinds of cells, oligodendrocytes and Schwann cells [4].

Active ongoing research in stem cells strives to show that transplantation of human embryonic stem cell derived endogenous oligodendrocyte progenitor cells (OPCs) into adult spinal cord within a short period of time following the injury enhances remyelination and promotes recovery of motor function. These OPCs that are recruited to an area of demyelination, differentiate into mature oligodendrocytes that wrap myelin around the demyelinated axons [31,4,21]. Animal models for MS and SCI, however, suggest that remyelination does not reach completion [33,36]. For this reason, many therapies are being developed to either enhance the amount of endogenous remyelination, or to introduce exogenous cells that are capable of remyelinating axons [8, 34,20]. One such treatment include the transplantation of oligodendrocyte progenitor cells into the adult spinal cord of rats within a short period of time following SCI. This therapy enhances remyelination and promotes recovery of motor function. However, to study the progress of the therapy these oligodendrocyte-remyelinated axons (OR-axons), created due to oligodendrocyte progenitor cell transplanta-

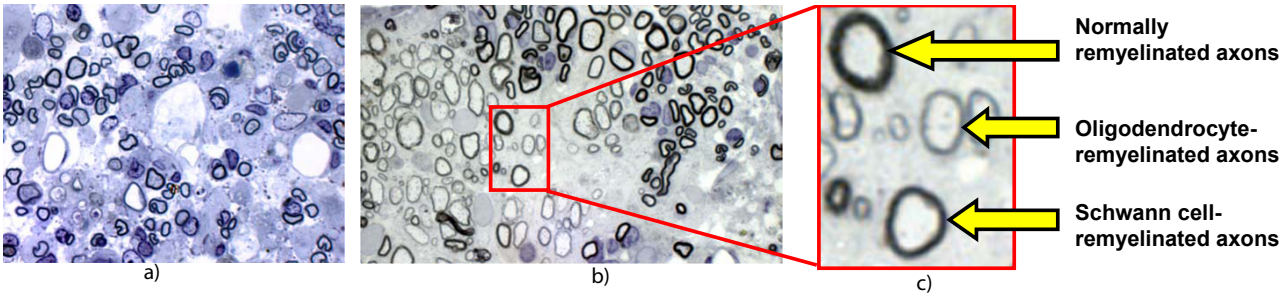

Fig. 1 Different kinds of cells in the image. Left and Middle show images obtained with different staining processes and hence the overall color difference. The right one is the zoomed in view of the middle image showing the different types of axons.

tion, need to be distinguished from the already myelinated axons or axons remylinated by the Schwann cells already existing in the body. The OR-axons are identified by their characteristically thin myelin sheaths relative to the diameter of the axons – when compared with the myelin sheath of the axons remyelinated othewirse. Thus, the ratio of myelin sheath thickness to axon diameter, G-ratio [36], needs to be analyzed to identify the OR-axons. Following the identification of OR-axons, their distribution has to be analyzed by visualizing the size, location and density of its clusters in the image. By tracking such visualizations of microscopic images periodically captured on different rat subjects before and after the treatment, one can understand the growth rate and site of the OR-axons and hence the effectiveness of the therapy.

1.1 Motivation

Remyelination is analyzed on microscopic images of $5 \times 625 \mu m^2$ areas aligned on a radially oriented line that originates from the central canal of the spinal cord and extends to the outermost limit of the spinal cord cross section. The current method for identifying remyelinated axons is the manual line sampling technique [5]. There are two kinds of error introduced in manually estimating and classifying the remyelinated axons. Since a manual process is very tedious, the OR-axons are only identified in approximately 15% of the actual area of pathology. In the rest of the area, it is only estimated. This leaves out a high percentage of the area introducing a large *estimation error*. Further, there is *classification error* because of the subjectivity involved in the manual classification of the OR-axons. Note that the parameter critical for classification, G-ratio, is a ratio of two thicknesses. It is usually hard to evaluate a ratio visually. This, is turn, makes it very tedious and time-intensive to estimate the G-ratio for every OR-axons. Hence, it is often assigned by relative measure through spatially local visual estimation. This leads to more classification errors. It is not known how much error is introduced to the data when there are multiple examiners counting these axons. These errors can be reduced by increasing the percentage of the actual area of pathology, but the sheer size of the number of samples collected from the pathology makes this a daunting task when performed manually. For example, since a microscopic slice is taken every 2mm of the spinal cord of an animal, in experiments involving many animals, the OR-axon growth analysis can take several weeks. An increase in percentage of counted area would not only increase the analysis time, but might also increase the error due to human factors such as fatigue.

An automated method to classify and visualize the distribution of the OR-axons can alleviate all the above problems and provide an incredibly useful analysis tool for research in these kinds of cutting edge therapies. An automated system will allow analysis of a higher percentage of area of the pathology, at more frequent intervals, and at higher accuracy due to less subjectivity and human factor related errors. Thus, it is evident that automated recognition, classification, and visualization of the axons would be imminent in reducing the turn-around-time and the subjective error in this research.

1.2 Technical Challenges

Automating the process of recognition and classification of the OR-axons and visualization of their distribution involves taking as input a microscopic image (Figure 1a) and creating a density map (Figure 10c,d) where blue regions indicate high density clustering of OR-axons. The complexity of this automation is compounded by the following facts.

- The microscopic image is littered with a large amount of 'cellular debris', i.e. proteins and other cell bodies that have to be identified and rejected, or not identified at all.
- The oligodendrocyte cells do not conform to any particular shape. In fact, even basic shape properties like convexity cannot be assumed. This demands a *shape independent* classifier to distinguish the cells.

– The average intensity level of the input images might be different depending on the staining process (Figure 1a and 1b). Hence relating intensities across images for consistently identifying the cells is not possible, and this intensity threshold for cell identification has to be learned within each image.

1.3 Main Contribution

Most existing methods for automatic cell analysis focus on large, cellular matrices [44]. However, in cases where the topology of the cellular structures is not uniform, as is typically the case in injury sites, methods for identification and quantification of individual cells must be employed. Our main contribution is in designing an end-to-end automated process that analyzes the input microscopic image and returns an effective high-level visualization of the distribution of the OR-axons. We present a robust algorithm to handle noise, subjectivity and under-sampling, by using efficient computational geometry and stable statistical techniques.Our method consists of the following five key steps.

1. *Contour Detection:* First, we detect the myelin sheath surrounding the axons using progressive isocontours at varying intensity levels (Section 3). This technique is a *shape independent* process that makes use of the variational property of the intensities of the cell structures. This also allows us to detect axon boundaries across images of different intensities and pathologies stained by different dyes.
2. *Contour Separation:* Since the contour detection step does not consider the shape of the axons, the boundaries detected by this step may include multiple axons. We use a Delaunay triangulation based method to separate these cells and define a clean and unique boundary for each of them (Section 4).
3. *Noise Removal:* The cells detected by the above steps may include noise (e.g. cellular debris). In this step, we identify this noise and remove the cells that do not represent axon structures (Section 5).
4. *OR-Axon Classification:* G-ratio is defined as the ratio of the cell boundary (myelin sheath) thickness to the cell diameter. The remyelination due to different cells can be differentiated by the G-ratio of the cell. In this step, we design a method based on G-ratio computation and clustering to identify the oligodendrocyte-remyelinated (OR)-axons from other axons (Section 6).
5. *Density Map Generation:* Finally, we use the distribution of the detected OR-axons in the image to generate a density map that is effective in visualizing the size, location and density of their clusters in the area of the pathology (Section 6.1).

The pipeline of the entire process, as described above, is illustrated in Figure 2. We corroborate our method by extensive cross-verification by the domain experts to demonstrate its accuracy and robustness.

We first discuss the relevant literature in Section 2. Then we present the four steps of our automated algorithm in Sections 3 to 6.1. This is followed by experiments and analysis in Section 7. Finally, we conclude in Section 8.

2 Related Work

Digital image cytometry [17,18,46], the analysis of cell attributes from images, serves as an essential component of biological research. Correct detection of relevant cell structure and boundaries is a challenging task in image cytometry because of the varying intensity levels in the images occurring from different staining protocols, varying sizes of the specimen, difference in shapes across cell structures and the presence of large numbers of cellular debris.

Cell detection algorithms using image processing and computer vision techniques continue to be a significant area of research [28,18,46,41,6,32,12,35,3,22,45,42]. Shape based analysis of cells is a common approach used by researchers [37,10,1] and is applicable to types of cells that conform to specific shapes. Since the OR-axons can be of any arbitrary shape, the shape dependent methods are not useful and shape invariant analysis must be used for detection, identification and classification of axons.

Watershed segmentation is a widely used shape-independent approach for cell detection [23,16,27], but this algorithm is susceptible to the presence of noise in the image. A single outlier can impact large groups of pixels thereby making the watershed segmentation unstable. Most cell detection algorithms usually detect some cell structures that are merged and need to be separated. Thus, segmentation or separation of cell boundaries to detect individual cells is an active area of research [30,19,7,18,46]. The active contours method [45,43,19,7,46] is successfully employed for cell analysis and usually produces robust boundaries even for noisy images. Zimmer et al. [46] use an active contour based cell segmentation approach to detect and track motile cells. They use an edge map computed from deviation between local intensities to detect low contrast boundaries. While active contours detects the cell structure by energy minimization subject to external and internal constraints, our proposed approach uses different contours of the same image to classify a structure as a cell by analyzing the evolution of boundaries detected by the isocontour algorithm progressively.

In almost all applications, the nature of staining makes the nuclei of cells more prominent compared to the outer cell boundaries. A good cell segmentation algorithm has to correctly identify the separating region between the adjacent

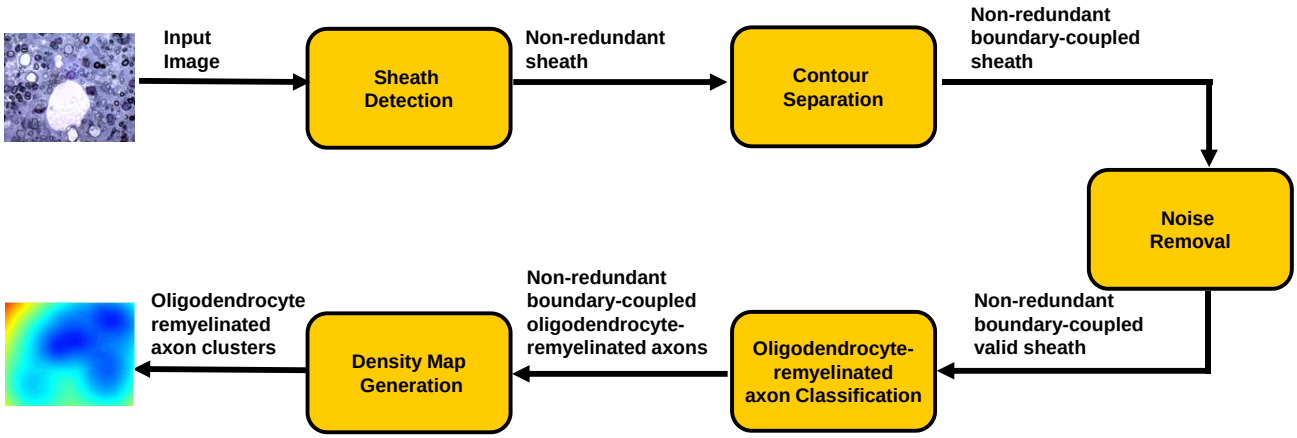

Fig. 2 The pipeline of our proposed algorithm.

cell nuclei. Using a known cell nucleus, Jones et al. [18] use non-Euclidean Voronoi diagrams on Riemannian manifolds to detect cell boundaries and segment cells. The cell nucleus is not known in our applications, and hence the approach proposed in [18] is not applicable to our problem. We use an Euclidean-space Delaunay triangulation based approach to separate the detected axon boundary contours obtained from progressive isocontouring. Furthermore, our method directly works on the geometry of the 2D cell structure provided by the isocontouring algorithm, while [18] works on higher dimensional space derived from the image parameters.

We introduce the concept of progressive isocontouring to detect all the cell structures followed by contour separation using Delaunay triangulation. This allows us to detect event points when there is a morphological change in the shape of the isocontours which can subsequenly be used in the post processing stage to detect generic cell structures. Similar computational geometry-based approaches to topology tracking include efficient implementations of Reeb graphs [11].[1] The detected cell structures, once identified as axons, are processed to identify the subset of OR-axons using robust geometrical and statistical methods.A shorter version of this method appears in [9].

3 Contour Detection

Traditionally, axon detection algorithms use two techniques – shape dependent analysis and edge detection. Since the OR-axons can be of any shape, typical shape matching algorithms cannot be used in our applications. Further, traditional edge detection methods also cannot be used due to the presence of an abnormal number of debris in the image, and the need for correct computation of relative size of the detected boundaries in order to classify the axons.

The OR-axons sometimes can be classified by their lighter intensity values in the image slices. The intensity value at which these axons can be detected can vary over the time elapsed from the remyelination procedure, and also depends on the subjective manual staining process before the microscopic images are taken. Hence isocontouring at one specific intensity level will not be a feasible solution for this problem.

We present the progressive isocontouring technique – isocontouring at progressively increasing intensity levels – as a generic method to detect possible axon structures. For this purpose, we first define the axon structure in this context as illustrated in Figure 3. Let us consider two simple closed iso-contours at intensity i – the inner contour $I(i)$ and the outer contour $O(i)$. Let these two enclose regions $A_I(i)$ and $A_O(i)$ respectively such that $A_I(i) \subset A_O(i)$. Then $A_O(i)$ constitutes an axon and the region between the contours $I(i)$ and $O(i)$, given by $A_O(i) - A_I(i)$, constitutes the myelin sheath $S(i)$. The thickness $T(i)$ of the sheath $S(i)$ is given by the average of the closest distances of every inner contour point to the outer contour. This is illustrated in Figure 3.

We compute iso-contours progressively at different intensity levels moving from lower to higher intensities. A sheath $S(i)$ detected at intensity level i signifies a valid structure if it obeys the rules described below. These rules are framed based on our observations of the structure of the axon and its surrounding myelin sheath in the images.

1. *Boundary Coupling:* There exists a one-to-one and onto relationship between the inner and outer boundaries of a sheath structure $S(i)$. This maintains the invariance that every inner boundary has a corresponding unique outer boundary and vice-versa.
2. *Non-Redundant Sheath Structure:* Since the myelin sheath is always darker than both the interior and exterior of the axon, the thickness of the sheath detected at

[1] Note that although the analysis of evolving topology and its events is also the basis of Morse theory [26], its application is limited in the context of medical image processing due to the complexity of the image content [15].

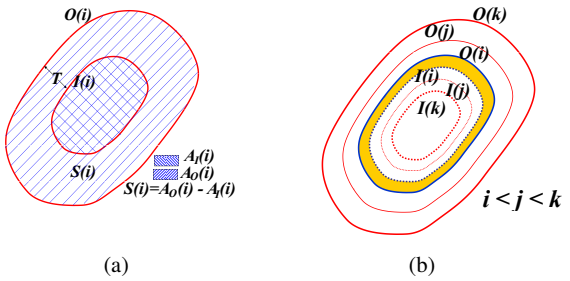

Fig. 3 (a) This schematic illustrates the axon and sheath structures in the image. (b) This illustrates the redundant sheath structures. The two redundant sheath structures are shown with red inner (dotted line) and outer (solid line) boundaries. The sheath structure shown in yellow with blue boundaries is the one detected at the lowest intensity and hence it is retained as the non-redundant sheath structure.

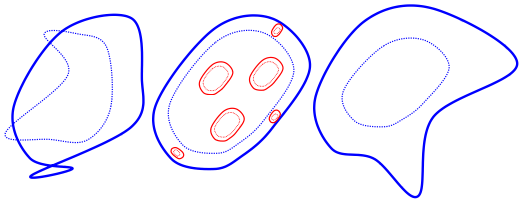

Fig. 4 This schematic shows all the invalid axons. Left: Invalid axons due to self-intersecting boundary or intersecting inner and outer boundary; Middle: Invalid axon due to axon-within-axon structure; Right: Invalid axon due to local discontinuity in sheath thickness.

the intensity level i will be less than that of the sheath detected for the same axon at a higher intensity level. Let $S(i) = A_O(i) - A_I(i)$ and $S(j) = A_O(j) - A_I(j)$ be the sheaths at intensity levels i and j, $i < j$ (Figure 3b). If $A_I(j) \subset A_I(i) \subset A_O(i) \subset A_O(j)$ then $T(i) < T(j)$. In this case both $S(i)$ and $S(j)$ represent the sheath of the same axon in the image detected at different intensity levels. In order to avoid double counting of axons, only one of them is retained and the other one is rejected. We retain the the sheath detected at the lowest intensity level in order to have a standardized reference to compare the sheath thickness across different axons in the same image for subsequent classification. We call this sheath structure $S(i)$ at the lowest intensity i as the non-redundant sheath structure.

3. *Valid Sheath Structure:* There are three rules of a valid axon structure. First, no axon can be inside another axon. Second, the inner and outer boundaries, $I(i)$ and $O(i)$, should not be self-intersecting or intersect with each other. Finally, the thickness T defined by the distance between $I(i)$ and $O(i)$ should be locally uniform across the entire boundary. Hence, the change in thickness, if existing, should be smooth.

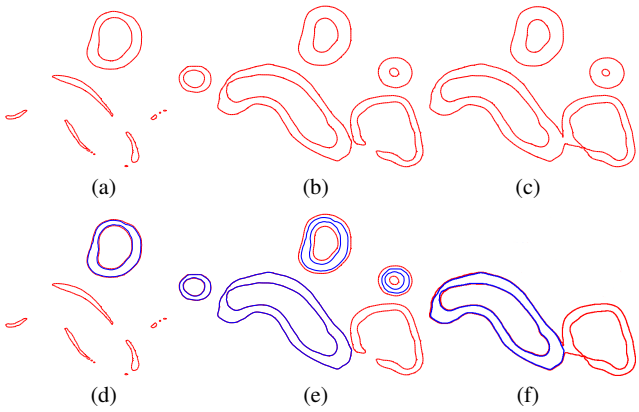

Fig. 5 Progressive Isoconturing on Real Data: isocontours of the image at three different intensity levels. The top row shows the isocontours at each intensity level, and the bottom row shows the identification of axon structures (shown in blue). The isocontours (d) have multiple components and as intensity level increases progressively, complete axon structures are formed (b), and valid axon structures get morphed and merged at still higher intensity levels (c,f). When complete axon structures are detected at a particular intensity level, its geometry is preserved (d-f) and hence it is not affected by the subsequent morphing of the isocontours.

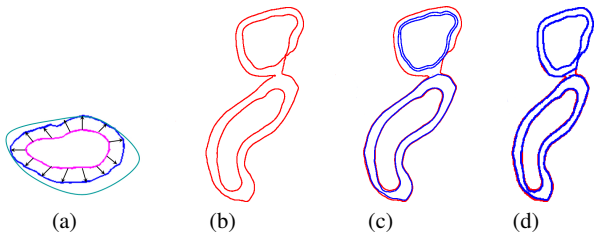

Fig. 6 (a) Contour dilation process on Real Data. (b-d)Problems with dilation based axon-separation. (b) The outer contour merges, even as the outer contour of one of the two sheaths has not been detected. (c) One of the inner contours that does not have a corresponding outer contour is dilated to the minimum distance between itself and the merged outer contour. Note the thickness is much smaller than the reasonably correct shape given by the red contour. Such problems will skew the G-ratio of this axon, and hence its classification. (d) Our Delaunay based separation algorithm computes the correct sheath shape.

We detect iso-contours using standard iso-contour algorithms. A contour is a closed polyline connecting a sequence of vertices. Next we perform a contour within contour test to decipher the inner and outer boundary contours. A contour I is within another contour O if all vertices of I are inside O. A vertex v is inside a closed contour O, if a ray shot from v to an arbitrary point well outside the bounding box of O intersects O an odd number of times. Hence the vertex-inside-a-closed-contour test needs a line-polygon intersection test. If a contour I lies inside another contour O, we identify I to be an inner boundary and O to be its corresponding outer boundary. We perform progressive isocontouring without violating the redundant sheath structures criterion by retaining the structure that is detected the earliest, as shown in Figure 5 on a typical situation. Note that there

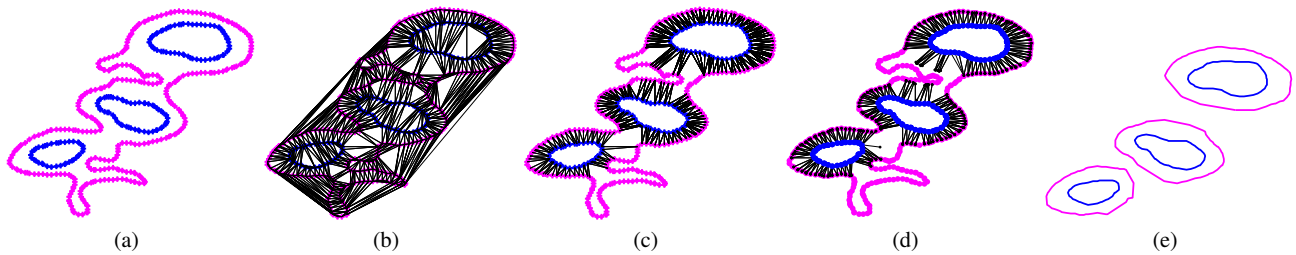

Fig. 7 Contour separation algorithm on Real Data: (a) The pink outer boundary encloses multiple blue inner boundaries violating the boundary coupling criterion. (b) The Delaunay triangulation of the vertices on inner and outer boundary contours. (b) The edges of the triangulation that connect any inner boundary vertex to an outer boundary vertex are retained. (d) The edges incident on each inner boundary that are statistical outliers with respect to edge length are shortened to match the average edge length of these edges. (e) The closed loop of vertices thus formed by the farther ends of the edges incident on each boundary forms the corresponding outer boundary thus separating the merged outer boundary contour.

can be multiple inner boundaries associated with a single outer boundary violating the boundary coupling criterion as shown in Figure 5c. These are handled in the contour separation step, as explained in Section 4. Further, there can also be multiple outer boundaries associated with a single inner boundary violating the valid sheath structure criterion. These are handled in the noise removal step, as explained in Section 5.

The isocontours at specific intensity levels show the regions of the axon in different topologies: the axon boundaries might have multiple components (Figure 5a) or multiple axons might be merged into a single axon boundary (Figure 5c). On the other hand an analysis of the change in topology of the axon boundaries over the isocontours of smoothly varying intensity levels provides a wealth of information for identifying the sheath structures accurately. This is the key observation behind the progressive isocontouring method. We compute the curves with the same brightness (isocontours) in the image repeatedly for progressively increasing intensity values (Figure 5). When the topology of the isocontour changes over subsequent higher intensity levels, we analyze it to detect the formation of new sheath structures (two closed curves one containing the other). These sheaths identified at a specific intensity level (blue curves in Figure 5d-f), would be enclosed by the isocontours in the subsequent intensity level images (red curves in Figure 5). These containments are detected and only the blue isocontours (with smaller sheath thickness) are retained as a non-redundant sheath structure.

4 Contour Separation

After the first step of the pipeline we get non-redundant sheaths, but they may not satisfy the boundary coupling criterion. There can be detected outer boundary contours that enclose multiple smaller inner boundary contours. This is due to the fact that any pathology being imaged by the microsope, though very thin, still has a non-zero thickness. Each cell seen in the image will have a slightly different depth than the others. Though their mobility is restricted, they can sometimes occlude parts of other cells merging visible outer boundaries.

Figure 7a illustrates the typical scenario of merged contours where the outer boundary of multiple myelin sheath structures are merged. This step of our algorithm divides the outer boundary into required numbers of closed curves to match with each enclosed inner boundary (Figure 7d). One simpler and obvious solution to separate the contours is by dilating the inner contour along the normal direction by the minimum distance to the outer contour enclosing it (Figure 6a). Although this method works reasonably well in many cases, it is not robust and is susceptible to noise (cellular debris) in the image. It may lead to sheath structures with inaccurate thicknesses and hence inaccurate G-ratio value and eventual misclassification of the OR-axons (Figure 6c).

To avoid these problems, we propose a robust Delaunay triangulation based contour separation algorithm. A triangulation of a point set is Delaunay if no point is inside the circumcircle of any triangle of the triangulation. Hence, a point is always connected to its closest point in Delaunay triangulation. Before detailing the algorithm, let us consider a sheath whose inner and outer boundaries, I and O are detected and coupled correctly. Let us consider a Delaunay triangulation of the vertices in the two boundaries, i.e. $I \cup O$. Let us retain only those edges from this triangulation that connect a point in the inner boundary to a point in the outer boundary. This retained set of edges corresponds to the sheath S in which all edges have lengths close to the thickness of the sheath (Figure 7). Further, we also notice empirically that all vertices in the outer contour are connected to at least one inner contour vertex. We use these observations to handle situations where there are multiple inner contours within a single outer contour (Figure 7a).

The contour separation method takes as input N, $N > 1$, inner contours, denoted by I_k, $1 \leq k \leq N$ and their single outer contour O. The output is N closed outer contours, O_k

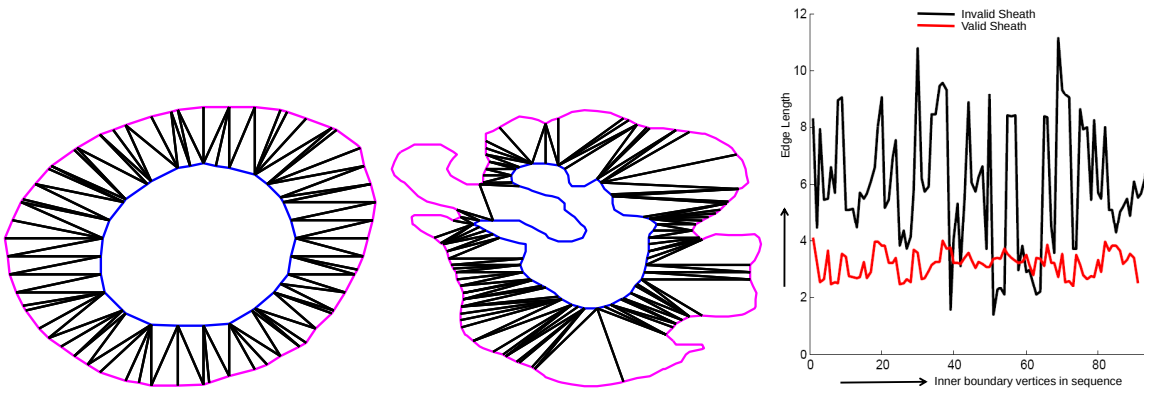

(a) (b) (c)

Fig. 8 This figure illustrates the local discontinuities in edge length in an invalid sheath when compared to a valid sheath in real data. a) and the b) show a valid and an invalid sheath respectively. c) shows the plot of the sheath thickness as we move along the contour of the valid and invalid sheath. The valid sheath shows a locally smooth plot while the bad cell shows severe local discontinuities.

one corresponding to each inner contour I_k, carved out of O. The basic observation is that around each inner contour I_k, the outer contour O is well formed except in areas of concavities in O (Figure 7a). For this we first perform a Delaunay triangulation of all the points in I_k, $1 \leq k \leq N$, and O (Figure 7b). Next, we retain the edges connecting the inner boundary vertices to the outer boundary vertices (Figure 7c). Note that the Delaunay edges in the concavities of O connect two outer boundary vertices and are hence removed.

As discussed earlier, in an ideal cell with coupled inner and outer boundary contours, the retained Delaunay edges incident on the inner boundary vertices are all of similar lengths. So, we find the edges incident on each I_k that are statistical outliers in terms of their length. These are usually the edges which couple an inner boundary vertex to an incorrect vertex in the outer boundary or a different inner boundary. If an outer boundary vertex p_o is connected only by these retained Delaunay edges that are statistical outliers then each of these edges connected to p_o is shortened away from p_o to the average length of all the other non-outlier edges incident on I_k (Figure 7d). The outer boundary O_k is now formed by connecting the farther end points of the edges incident on I_k in order (Figure 7e).

This Delaunay based contour separation method is extremely robust. This algorithm is also provably correct as it retains only those Delaunay triangles whose circumcenter is close to the medial axis [2] formed by the coupled inner-outer contour pair points, thus establishing the one-to-one and onto correspondence between the inner and outer contours as prescribed by the boundary coupling criteria for the definition of a sheath structure. Further the lengths of the edges retained in this Delaunay triangulation provide a very good estimate of sheath thickness which is later used in our G-ratio computation and classification (Section 6).

5 Noise Removal

Following the contour separation step, we get non-redundant boundary coupled sheath structures, but we still have many invalid sheath structures detected due to cellular debris. In this step we identify such cellular debris and remove them. After the removal of cellular debris, the remaining cell structures satisfy all the rules of a valid axon structure described in Section 3.

Sheath structures that have self-intersecting boundaries and intersecting inner and outer boundaries can be identified using simple line-polygon intersection algorithms and removed. The invalidity due to axon-within-axon (Figure 4) is detected using the same contour within contour test as used to differentiate inner boundaries from outer boundaries in Section 3. Note that axon-within-axon noise structures are different from structures that require axon separation. The former structure has multiple axons (with both inner and outer contours) inside another axon (again with both inner and outer contours), while the latter has multiple inner contours inside a single outer contour.

The last case of invalid sheath structure is one with locally non-uniform sheath thickness. This is detected using an algorithm similar to the one proposed for contour-separation. We retain the Delaunay edges of the vertices in the inner (I) and outer (O) contours. The lengths of these edges in sequence should be locally smooth for valid sheath while invalid sheath structures would have severe local discontinuity. We demonstrate the invalid sheath structure using a typical example showing a valid and invalid structure in Figure 8. It can be clearly seen from a typical example in Figure 8c that the variance in the edge lengths of the valid and invalid sheaths are clearly different and can be used to distinguish one from the other.

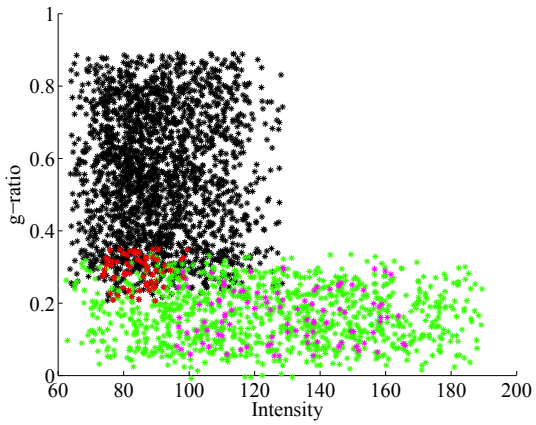

Fig. 9 K-means clustering algorithm for Axon Classification: The Y-axis shows the G-ratio of the axons. The X-axis is the intensity level at which specific axons were detected using the progressive isocontour process. The greeb points represent the OR-axons (true positives), the magenta, red and black points represent the false positives, false negatives and true negatives respectively. The data is accumulated over many microscopic images spanning different staining intensities, and with different numbers of axons.

6 OR-Axon Classification and Visualization

The identification and classification of oligidendrocyte-remyelinated axons are done based on a parameter called G-ratio. The G-ratio is defined as the ratio of the sheath thickness to the axon diameter. To find the sheath thickness, we perform the Delaunay triangulation of its inner and outer boundary vertices and retain only the edges that connect the inner boundary vertices to the outer boundary vertices. The mean length of these retained edges approximates the sheath thickness. The axon diameter is computed as the largest distance between any two points in the inner boundary I. There are three kinds of myelinated axons: (a) normally myelinated axons are those that were not affected during the spinal cord injury, (b) the axons that were remyelinated by the Schwann cells and (c) the axons that were remyelinated by the oligodendrocyte cells that were injected in the course of therapy. Our goal is to detect and count the OR-axons in order to monitor the progress of oligodendrocyte based remyelination which is a critical step in estimating the efficacy of the therapy. Oligodendrocyte remyelinated axons are characterized by lower G-ratios than the normally or Schwann remyelinated axons. Hence, to classify these therapeutically important axons we perform k-means clustering of the G-ratios with number of clusters set to two. The axons corresponding to the cluster with lower G-ratio are the OR-axons.

Since, typically during manual counting, it is prohibitively tedious to measure G-ratios for all the detected sheaths, the conventional way to identify an OR-axon is by the lighter intensity of its myelin sheath when compared to the darker, more compact, Schwann cell-remyelinated axons [36, 14]. Since we can accurately measure G-ratio automatically, we use this for clustering the OR-axons. However, we make an interesting observation from this classification. While it is true that all cells with lighter intensity sheaths are OR-axons, the converse is not true – not all OR-axons have lighter intensity sheaths. Hence, intensity based manual classification is prone to errors. Further, the intensity levels at which the axons are detected change based on the staining process before the microscopic images are taken. This makes intensity based manual classification subjective. Our automated G-ratio based classification thus reduces classification errors significantly.

The results of this clustering method for several images are shown in Figure 9. In this figure we plot the G-ratio of the axons (Y-axis) against the intensity levels (X-axis) of the progressive isocontouring algorithm at which the axon was detected. The image shows the plot of cells in over 15 images with variable staining intensity and different number of recognizable cells. Aggregated statistics from all these images are the following: all the cells recognized at an intensity level above 130 are oligodendrocyte remyelinated axons – so are all the cells with G-ratio below 0.2. Further all the cells with G-ratio above 0.35 are non-oligodendrocyte myelinated axons. The region of confusion is in the rectangular range of intensity less than 130 and the G-ratio between 0.2 and 0.35. The blue points in the figure denote the OR-axons and the black points mark all other cells. The false positives and false negatives are shown in magenta and red respectively. Further analysis of these results is given in Section 7.

6.1 Density Map Generation

To evaluate the effectiveness of the remyelination therapy it is important to identify the regions of the image where large clusters of high density OR-axons occur. The size and density of these clusters indicate the rate of progress and the location indicates the appropriateness of the targeted cite of the therapy.

To facilitate this process we calculate a density map as follows: the centroids of all the detected OR-axons are identified, and for each pixel in the image, the average distance to its k nearest centroids are calculated. Color coding of these values gives the *density image* that visually represents the relative concentration of the detected cells. Lower values indicate higher concentration of OR-axons and vice versa. Hence, cooler colors (blue) indicate the cites of remyelination due to oligodendrocytes and warmer colors (yellow and red) indicate lack thereoff. Figure 10 shows the density maps thus calculated for the corresponding input images shown in the same Figure.

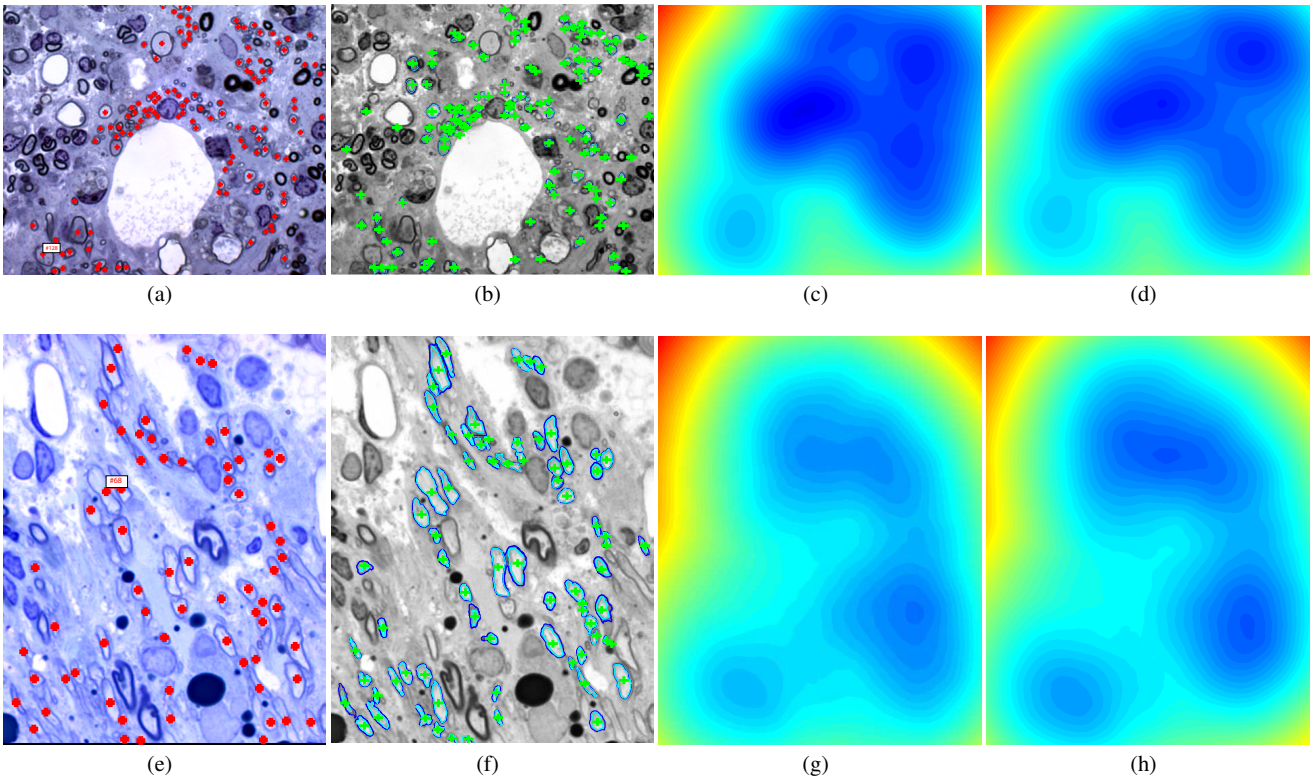

Fig. 10 (a),(e) Images shows the manual count of OR-axons represented using red markers. (b), (f) Automatic count of oligodendrocyte-remyelinated axons on the same images, using the algorithm presented in this paper. (c), (g) Visualization of the cluster density map of the manual counts (d), (h) Density map of the automated counts. Density images(c),(d) and (g),(h) should be similar if the actual and the manual counts closely match. Using image similarity measure SSIM [38], we show that the two pair of density images are indeed very similar (SSIM =0.982, 0.993).

7 Results and Analysis

We used Sprague Dawley female adult rats with 200 Kilo-Dyne force spinal cord contusion injury. All tissues were fixed and processed as described in [36]. The images of these tissues were used as input to our system. The implementation of the algorithm was prototyped using MATLAB and the images used had different intensities. The shapes and scales of the cells also varied across images. The remyelination analysis that we automated was also carried on manually by experts without the knowledge of the results of the automated process. The experts were also consulted to review the results of the automated process.

Sample classification results with manual count and automatic counts are demonstrated in Figures 13,14. The left column of the figures denote the greyscale images with manual counts marked with red and the right column denotes the results from our automatic classification with the detected cells marked in green. Figure14 demonstrates that our technique works for images with dense clusters of OR-axons as well as sparse clusters. Figure 11 shows a sample result of our automatic classification with false negatives denoted by red and false positives by magenta.

Additional results of the manual and automatic counts are shown in Table 1. Although manual counting by experts suffers from classification error due to the subjective nature of the task, all the statistics and analysis has been done assuming that the expert counting for the first time (before seeing the results of the automated process) is the ground truth (Column 1 of Table 1). The same images were then processed using our method and the automatic count of OR-axons were reported in Table 1. Correctly classified OR-axons were considered to be true positives (denoted by green in Figure 9), and the cells that are chosen by the system but not by the experts are false positive (denoted by magenta in Figure 9).

Actual count of axons	Automated count of axons	Hit rate	Excess rate
68	65	94.12	1.4
78	80	92.31	10.2
96	100	91.67	12.5
35	38	94.29	14.28
25	30	96	24

Table 1 Empirical performance evaluation using domain expert's count as ground truth: OR-axons detected by our algorithm closely match the ground truth, demonstrated by the high hit rate.

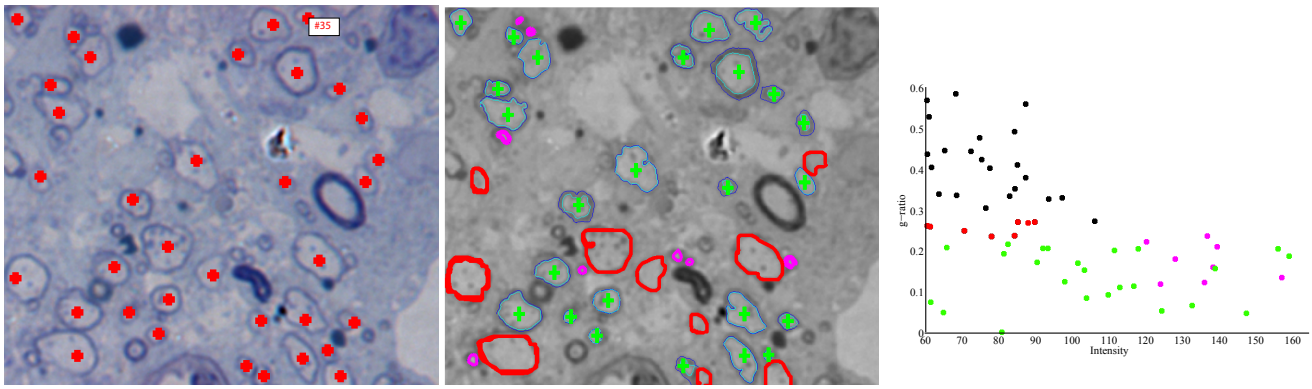

(a) (b) (c)

Fig. 11 (a) Manual classification (b) Automatic classification: False positives are shown in magenta, false negatives in red and true positives with green markers as compared to image (a). (c) Shows the k-mean classification of the cells. Note that the false negatives are in the boundary of true positives and true negatives and hence are difficult to automatically label them correctly using only G-ratio and intensity classifiers.

Traditionally, the success of an automated method is defined by the *hit rate* given by

$$\text{hit rate} = \frac{\text{Number of true positives}}{\text{Manual count of OR axons}}. \quad (1)$$

This is usually accompanied by a *false alarm rate* given by

$$\text{false alarm rate} = \frac{\text{Number of false positives}}{\text{Manual count of non-OR axons}}. \quad (2)$$

However, since the non-OR axons are of no importance in the context of remyelination, manual count for non-OR cells are not available for us to calculate false alarm rate. Hence, we define a new term called excess rate as

$$\text{excess rate} = \frac{\text{Number of false positives}}{\text{Manual count of OR axons}}. \quad (3)$$

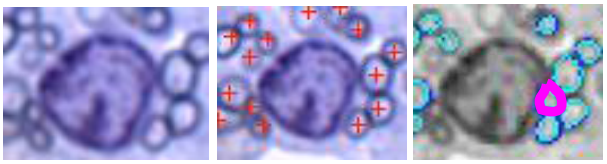

(a) (b) (c)

Fig. 12 False detection:(a) shows the original image, (b) the manual classification and (c) automatic classification. A typical falsely detected cell occurs when the algorithm combines neighbouring cell boundaries.

A high hit rate signifies effective classification of OR axons while a low excess rate signifies effective rejection of non-OR axons. Hence, the hit rate together with the excess rate provides an important indicator for the accuracy of the automated remyelination analysis. A high hit-rate ($> 90\%$) accompanied by a low excess rate ($< 25\%$) signifies a successful automated analysis.

The false positives (shown in magenta in Figure 9) either have high intensity or have very low G-ratio values indicating that they are indeed within the statistical range of correct OR-axons. Interestingly, on showing the results of the automatic cell detection, the experts concurred that over 95% of false positives (cells chosen by us but not the experts) were actually true positives. These true positives were missed due to several human factors like subjectivity and fatigue. This demonstrates the need for automated analysis and also validates a higher accuracy for our automated analysis by increasing the hit rates and reducing the excess rates.

On rare occasions, our algorithm falsely detects non-cell structures examples of one such false positive is shown in Figure 12. Our automated technique identifies the region enclosed by the boundaries of the neighboring cells as an independent cell as seen in Figure 12. In such occasions, this contributes to inaccurate computation of false positives.

On the other hand, the false negatives (shown in red) which determines the miss rate (i.e. 1-*hit rate*), in Figure 9, is in the boundary of true positives (shown in green) and true negatives (shown in black) and hence are difficult to automatically label them correctly using only G-ratio and intensity. A similar pattern is observed when considering single images, as shown in Figure 11. A couple of false negative cells are due to partial cell structures in the image and their cell boundaries are not closed contours. Hence our cell identification algorithms failed to detect cells with such incomplete information. Interestingly, classification of the false negatives was also subjective among human experts and the misclassification by the automated system is well within the variance experienced in human counting.

The most important validation of the success of the automated analysis would be in comparing a density map generated from the clusters created by the automated process with the one that is created from the clusters marked by the manual process since this is the visualization that is ultimately

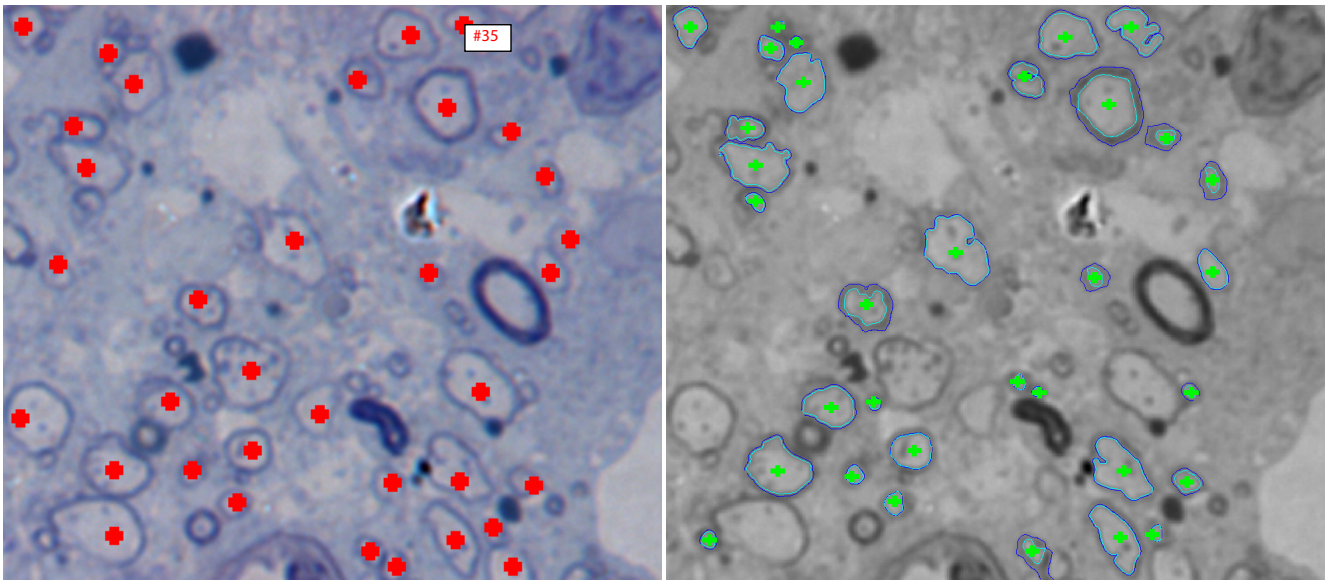

(a) (manual: 35; automated: 33)

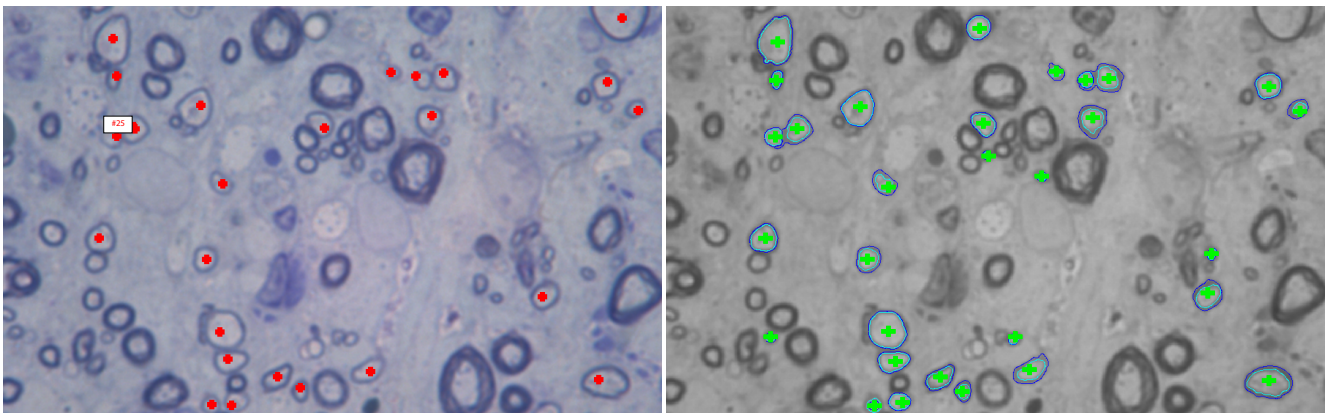

(b) (manual: 25; automated: 30)

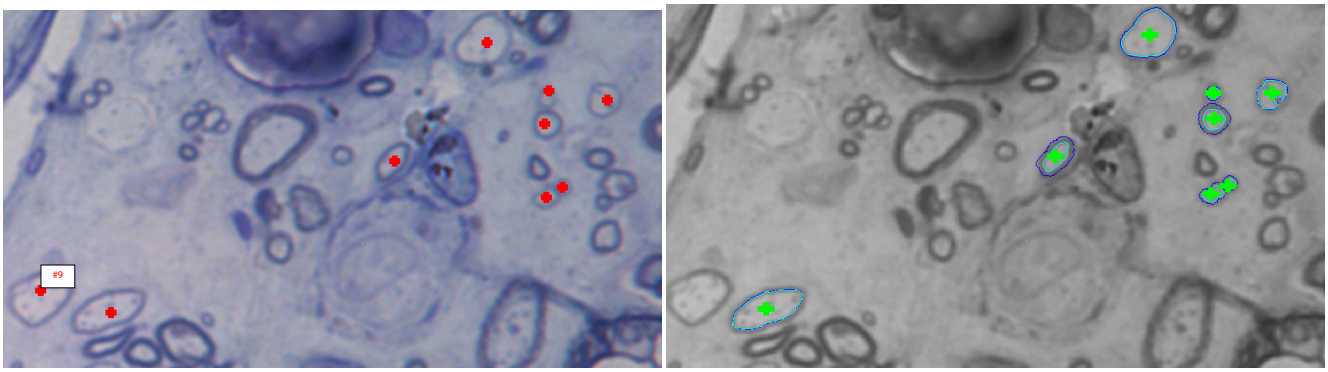

(c) (manual: 9; automated: 8)

Fig. 13 Classification results: Left: Stained images showing manual classification by domain experts; Right: Gray images showing classification using our automated method. The caption shows the number of OR-axons classified manually and automatically. Note that the domain experts nor the automated algorithm were aware of each others classification results. Please zoom in to see results.

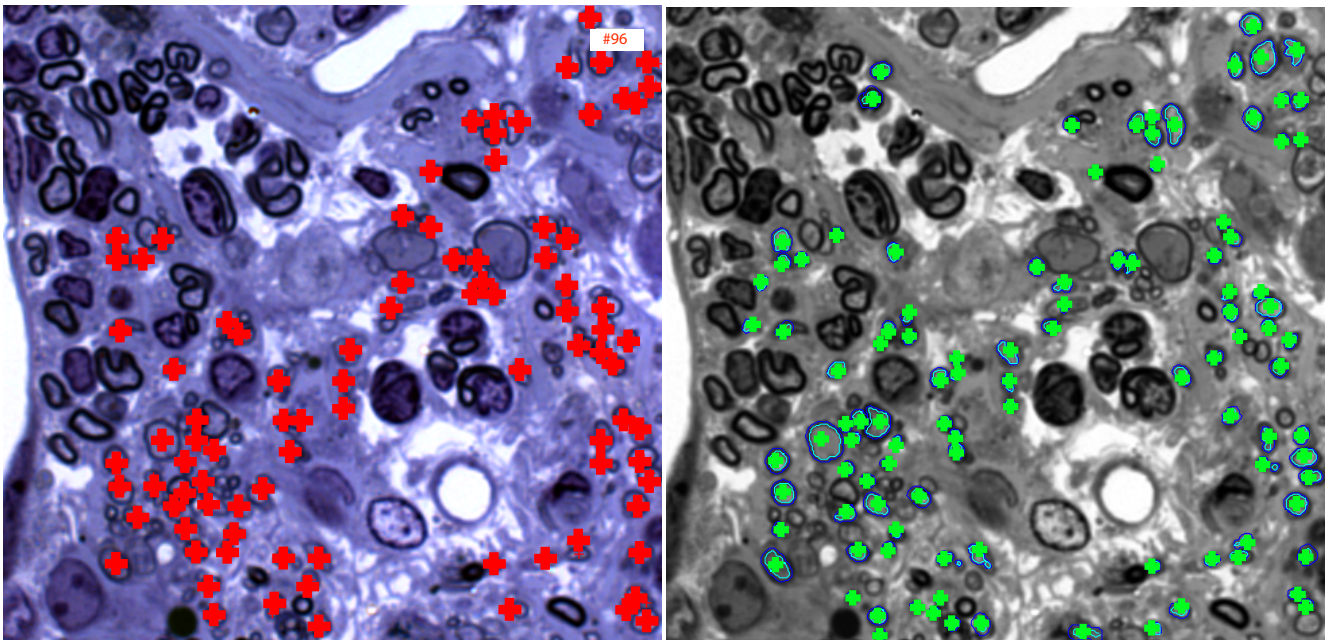

(a) (manual: 96; automated: 103)

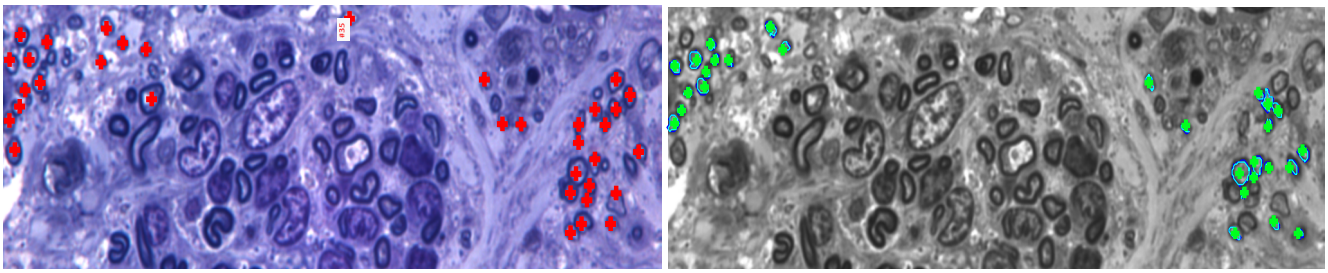

(b) (manual: 35; automated: 27)

Fig. 14 Additional classification results: Left: Stained images showing manual classification by domain experts; Right: Gray images showing classification using our automated method. The caption shows the number of OR-axons classified manually and automatically. Note that the domain experts nor the automated algorithm were aware of each others classification results. Please zoom in to see results.

used for detecting the growth and site of remyelination. Figure 10 shows examples of density images for both manual counts and automatic counts for two sample images. The number of k nearest neighbors was fixed at $1/4^{th}$ of the number of cells in the manual count. Blue regions in the density images denote areas having higher density of detected cells (Figures 10c, 10d and 10g, 10h). Note that figures 10 e,f contain OR-axons which are quite different in shape from the other OR-axons shown in the paper. Our algorithm is quite efficient in detecting these cells demonstrating that our technique is indeed shape-independent.

In order to quantify the image similarity between the density images from the manual and automated counts, we use a well established image similarity measure, Structural SIMilarity (SSIM) index [38]. SSIM is an objective method for assessing perceptual image quality using structural similarity between images. The mean SSIM index value of 1.0 between two images denotes two identical images. For the images shown in Figure 10, the mean SSIM index values between the density images corresponding to manual and automated counts is 0.982 and 0.993 respectively. The mean SSIM index for all the images reported in Table 1 is 0.97($\pm$0.02). Thus the method not only counts the desired cells with high degree of accuracy, but also identifies, classifies, and labels individual axons with very high confidence.

8 Conclusion and Future Work

We have presented an end-to-end process for accurate analysis and visualization of the clusters of OR-axons critical to evaluate the progress of remyelination therapy. Our automated cell classification always correctly identifies the region populated by the OR-axons, and closely matches the manual classification. Furthermore, the automated identification has a natural advantage of objectively classifying the axons. This automated remyelination analysis and visualiza-

tion has also injected a lot of excitement among our neurobiologist collaborators. This project will relieve them of several weeks of a pain-staking, repetitive, and mundane task that consumes several hours of trained manpower. By virtue of its accuracy in detection and classification of axons, we hope this method will find widespread applicability [25] thus reducing the turnaround time of the neurobiology research.

Our current application classifies cells as OR-axons and other cells. In future we plan to extend our application to classify cells into three categories, OR-axons, normally remyelinated axons and Schwann cells. Visualizing the three different type of myelination after the spinal cord injury will aid the biologists in analysing the effect of demyelination and remyelination, both natural and therapeutic, at the site of injury in a detailed manner. We are regularly interacting with our neurobiologist collaborators to improve our algorithm further to aid them in analysing the efficacy of the remyelination therapy. One possible option is to provide an interactive version of our application whereby the user can have the option of accepting the results of automatic classification or they can vary the threshold of the g-ratio to further improve the cell classifications. An alternative semi-automatic version of our algorithm could also provide the user the option to select a few sample axons belonging to each category, and the final classification is based on the sample cells they select. Currently, the code is prototyped in matlab and in future we plan to develop a complete package which can be used as a plugin with the microscope. Thus, the neurobiolists will have an united platform whereby they can visualize the remyelinated axons along with the microscopic images and track such visualizations of images periodically from the date of injury.

Though specific in application, there are several components of the algorithm that are generic and can be applied in different types of medical image analysis and visualization. The progressive isocontouring algorithm is a simple and generic image processing technique that can detect closed shapes in general stained microscopic images. In addition, this method also detects event points when the shape topology changes. Any application specific post-processing method can process just these events to detect the required cells. Our Delaunay triangulation based geometric processing contour separation and noise removal methods might evoke great interest in the newly developing bio-geometry community.

References

1. A. Aguado, M. Nixon, and M. Montiel. Parameterizing arbitrary shapes via fourier descriptors for evidence-gathering extraction. *CVIU*, 69:202–221, 1998.
2. N. Amenta, M. Bern, and D. Eppstein. The crust and the β-skeleton: Combinatorial curve reconstruction. *Graphical Models and Image Processing*, 60(2):125 – 135, 1998.
3. J. Angulo and G. Flandrin. Automated detection of working area of peripheral blood smears using mathematical morphology. *Anal Cell Pathol*, 25(1):37–49, 2003.
4. W. Blakemore and H. Keirstead. The origin of remyelinating cells in the central nervous system. *J Neuroimmunol*, 98:69–76, 1999.
5. A. Blight. Cellular Morphology of Chronic Spinal Cord Injury in the Cat: Analysis of Myelinated Axons by Line-Sampling. *Neuroscience*, 10:521–543, 1983.
6. R. Cahn, R. Poulsen, and G. Toussaint. Segmentation of cervical cell images. *J. Histochem. Cytochem.*, 25(7):681–688, 1977.
7. V. Caselles, F. Catte, T. Coll, , and F. Dibos. A geometric model for active contours in image processing. *Numer. Math*, 66-4:1–31, 1993.
8. D. Chari and W. Blakemore. New Insights into Remyelination Failure in Multiple Sclerosis: Implications for Glial Cell Transplantation. *Mult Scler*, 8:271–277, 2002.
9. K. Das, A. Majumder, M. Siegenthaler, H. Keirstead, and M. Gopi. Automated analysis of remyelination therapy for spinal cord injury. In *Proceedings of the Seventh Indian Conference on Computer Vision, Graphics and Image Processing*, ICVGIP '10, pages 314–321, New York, NY, USA, 2010. ACM.
10. C. Daul, P. Graebling, and E. Hirsch. From the hough transform to a new approach for the detection and approximation of elliptical arcs. *CVIU*, 72:215–236, 1998.
11. H. Doraiswamy and V. Natarajan. Efficient algorithms for computing reeb graphs. *Comput. Geom. Theory Appl.*, 42(6-7):606–616, 2009.
12. A. Garrido and N. P. de la Blanca. Applying deformable templates for cell image segmentation. *Pattern Recognition*, 33(5):821 – 832, 2000.
13. T. Goto and Y. Hoshino. Electrophysiological, histological, and behavioral studies in a cat with acute compression of the spinal cord. *J Orthop Sci*, 6:59–67, 2001.
14. J. Guy, E. A. Ellis, K. Kelley, and G. M. Hope. Spectra of G-ratio, myelin sheath thickness, and axon and fiber diameter in the guinea pig optic nerve. *J Comp Neurol*, 287:446–454, 1989.
15. A. Gyulassy, P.-T. Bremer, B. Hamann, and V. Pascucci. A practical approach to morse-smale complex computation: Scalability and generality. *IEEE TVCG*, 14, 2008.
16. D. Hagyard, M. Razaz, and P. Atkin. Analysis of watershed algorithms for greyscale images. In *ICIP*, pages III: 41–44, 1996.
17. A. J. Herzberg, B. J. Kerns, S. V. Pollack, and R. B. Kinney. DNA image cytometry of keratoacanthoma and squamous cell carcinoma. *Journal of Investigative Dermatology*, 97:495–500, 1991.
18. T. Jones, A. Carpenter, and P. Golland. Voronoi-based segmentation of cells on image manifolds. *ICPR*, 2:286–289, 2002.
19. M. Kass, A. Witkin, and D. Terzopoulos. Snakes - active contour models. *International Journal of Computer Vision*, 1-4:321–331, 1987.
20. H. Keirstead. Stem cells for the treatment of myelin loss. *Trends Neurosci*, 28:677–683, 2005.
21. Y. Li, P. Field, and G. Raisman. Death of oligodendrocytes and microglial phagocytosis of myelin precede immigration of schwann cells into the spinal cord. *J Neurocytol*, 28:417–427, 1999.
22. L. Liu and S. Sclaroff. Medical image segmentation and retrieval via deformable models. In *Proc. International Conference on Image Processing*, volume 3, pages 1071–1074, Oct. 7–10, 2001.
23. N. Malpica, C. O. de Solrzano, J. J. Vaquero, A. Santos, I. Vallcorba, J. M. Garca-Sagredo, and F. del Pozo. Applying watershed algorithms to the segmentation of clustered nuclei. *Cytometry*, 28(4):289–297, Aug 1997.
24. D. McTigue, P. Horner, B. Strokes, and F. Gage. Neurotrophin-3 and brain-derived neurotrophic factor induce oligodendrocyte proliferation and myelination of regenerating axons in the contused adult rat spinal cord. *J Neurosci*, 18:5354–5365, 1998.

25. J. Meyer, K. Velasco, and M. Gopi. Tracking of oligodendrocyte remyelinated axons in spinal cords. In *AIChE(Poster)*, 2008.
26. J. Milnor. *Morse Theory*. Princeton University Press, 1969.
27. L. Najman and M. Schmitt. Geodesic saliency of watershed contours and hierarchical segmentation. *T-PAMI*, 18:1163–1173, 1996.
28. J. Park and J. Keller. Snakes on the watershed. *IEEE Transactions on Pattern Analysis and Machine Intelligence*, 23(10):1201–1205, Oct 2001.
29. J. Prineas. Pathology of the early lesion in multiple sclerosis. *Hum Pathol*, 6:531–534, 1975.
30. B. S. Watershed, hierarchical segmentation and waterfall algorithm. In *Mathematical Morphology and its Applications to Image Processing*, pages 69–76, 1994.
31. H. Salgado-Ceballos, G. Guizar-Sahagun, A. Feria-Velasco, I. Grijalva, L. Espitia, A. Ibarra, and I. Madrazo. Spontaneous long-term remyelination after traumatic spinal cord injury in rats. *Brain Res*, 782:126–135, 1998.
32. F. Schnorrenberg, C. Pattichis, K. Kyriacou, and C. Schizas. Computer-aided detection of breast cancer nuclei. *IEEE Transactions on Information Technology in Biomedicine*, 1(2):128–140, June 1997.
33. N. Scolding and R. Franklin. Remyelination in demyelinating disease. *Baillieres Clin Neurol*, 6:525–548, 1997.
34. M. Strangel and H. Hartung. Remyelinating strategies for the treatment of multiple sclerosis. *Prog Neurobiol*, 68(361-376), 2002.
35. J.-P. Thiran and B. Macq. Morphological feature extraction for the classification of digital images of cancerous tissues. *IEEE. J. Biomed. Engg*, 43(10):1011–1020, Oct. 1996.
36. M. Totoiu and H. Keirstead. Spinal cord injury is accompanied by chronic progressive demyelination. *J Comp Neurol*, 486(373-383), 2005.
37. D. Tsai. An improved generalized hough transform for the recognition of overlapping objects. *IVC*, 15:877–888, 1997.
38. Z. Wang, A. C. Bovik, H. R. Sheikh, and E. P. Simoncelli. Image quality assessment: From error visibility to structural similarity. *IEEE Transactions on Image Processing*, 13(4):600–612, 2004.
39. S. Waxman. Demyelination in spinal cord injury. *J Neurol Sci*, 91(1-14), 1989.
40. S. Waxman. Demyelination in spinal cord injury and multiple sclerosis: what can we do to enhance functional recovery? *J Neurotrauma*, 9:S105–117, 1992.
41. D. Wu and Q. Zhang. A novel approach for cell segmentation based on directional information. In *ICBBE 2007*, pages 920–923, July 2007.
42. H. S. Wu, J. Barba, and J. Gil. Iterative thresholding for segmentation of cells from noisy images. *J Microsc*, 197(Pt 3):296–304, Mar 2000.
43. C. Xu and J. L. Prince. Snakes, shapes, and gradient vector flow. *IEEE Transactions on Image Processing*, 7(3):359–369, 1998.
44. X. Zhou, X. Cao, Z. Perlman, and S. T. C. Wong. A computerized cellular imaging system for high content analysis in monastrol suppressor screens. *J. of Biomedical Informatics*, 39(2):115–125, 2006.
45. C. Zimmer, E. Labruyere, V. Meas-Yedid, N. Guillen, and J.-C. Olivo-Marin. Segmentation and tracking of migrating cells in videomicroscopy with parametric active contours: a tool for cell-based drug testing. *IEEE. J. Med. Imaging*, 21(10):1212–1221, Oct. 2002.
46. C. Zimmer, E. Labruyere, V. Meas-Yedid, N. Guillen, and J.-C. Olivo-Marin. Improving active contours for segmentation and tracking of motile cells in videomicroscopy. *Computer Vision for Biomedical Image Applications(poster)*, 3765, 2005.